Materials Science in Semiconductor Processing 42 (2016) 188–195

Contents lists available at ScienceDirect

Materials Science in Semiconductor Processing

journal homepage: www.elsevier.com/locate/mssp

Defect evolution and dopant activation in laser annealed Si and Ge

F. Cristiano [a,*], M. Shayesteh [b], R. Duffy [b], K. Huet [c], F. Mazzamuto [c], Y. Qiu [a,1], M. Quillec [d], H.H. Henrichsen [e], P.F. Nielsen [e], D.H. Petersen [f], A. La Magna [g], G. Caruso [h], S. Boninelli [g]

[a] LAAS, CNRS and Université de Toulouse, 7 av. Du Col. Roche, 31400 Toulouse, France
[b] Tyndall National Institute, University College Cork, Lee Maltings, Cork, Ireland
[c] LASSE DaiNippon Screen, 13-21 Quai des Gresillons, 92230 Gennevilliers, France
[d] Probion Analysis, 37 rue de Fontenay, 92220 Bagneux, France
[e] CAPRES A/S, Kongens Lyngby 2800, Denmark
[f] Department of Micro- and Nanotechnology, DTU Nanotech, Technical University of Denmark, Kongens Lyngby 2800, Denmark
[g] CNR-IMM, VIII Strada and Via S. Sofia 64, 95100 Catania, Italy
[h] Dip. Di Fisica ed Astronomia, Univ. Di Catania, Via S. Sofia 64, 95123 Catania, Italy

ARTICLE INFO

Article history:
Received 13 July 2015
Received in revised form
7 September 2015
Accepted 8 September 2015
Available online 26 September 2015

Keywords:
Laser thermal annealing
Extended defects
Transmission electron microscopy
Ion implantation
Dopant activation

ABSTRACT

Defect evolution and dopant activation are intimately related to the use of ion implantation and annealing, traditionally used to dope semiconductors during device fabrication. Ultra-fast laser thermal annealing (LTA) is one of the most promising solutions for the achievement of abrupt and highly doped junctions. In this paper, we report some recent investigations focused on this annealing method, with particular emphasis on the investigation of the formation and evolution of implant/anneal induced defects and their impact on dopant activation. In the case of laser annealed Silicon, we show that laser anneal favours the formation of "unconventional" (001) loops that, following non-melt anneals, act as carrier scattering centres, leading to carrier mobility degradation. In contrast, in the case of melt anneals, the molten region itself is of excellent crystalline quality, defect-free and with very high activation rates. As for laser annealed Germanium, we studied in detail the amorphous to crystalline Ge phase transition as a function of the increasing LTA energy density and we found that using LTA, very high carrier concentrations (above 10^{20} cm^{-3}) were achieved in As doped regions, which are unachievable with conventional rapid thermal annealing (RTA) processes.

1. Introduction

During the last decade, the miniaturisation of planar "bulk Si" MOSFETs (Metal-Oxide-Semiconductor Field Effect Transistors) through the "traditional" geometrical scaling approach has become extremely difficult, due to the uncontrolled increase of short channel effects (and consequently of power consumption) [1]. Several solutions were developed to mitigate such effects (high-k/metal gate, strain engineering, ultra-thin Silicon-on-Insulator (SOI) substrates, 3D nano-fabrication…), which could be eventually combined into one technology process. As a consequence, a considerable diversification of the possible device architectures for future nodes occurred: today, the most advanced MOS device architectures range from (still) planar Fully-Depleted (FD)-SOI transistors, to 3D multigate FinFETs or gate-all-around nanowire (NW)-FETs (cf. Fig. 1). Doping requirements of source/drain (S/D) regions may therefore differ depending on the specific device architecture.

In modern FD-SOI technology, the doping of the raised source/drain (RSD, or High-Doped Drain, HDD) is achieved *in situ* during the growth of the RSD layer, while the use of ion implantation for S/D extension doping (or Low-Doped Drain, LDD) is a major technological challenge, considering the need to achieve a controlled lateral diffusion/abruptness, with limited damage in a nanometric layer [2,3]. Additionally, novel approaches based on ion implantation have been proposed for the control of the "extrinsic" resistance components of the S/D module (silicide, Schottky barrier height and contact metal). These include the use of ultra-low energy implants to increase the dopant concentration at the semiconductor/silicide interface [4] or the segregation of implanted dopants to lower the Schottky Barrier height [5,6].

Additional critical issues need to be considered for 3D FinFETs. One is the reduction of damage formation during annealing, which is impossible to avoid when amorphisation occurs during the implant [7]. To this respect, high-temperature "hot" implants [8] have been proposed to reduce damage accumulation during the implant. The second is conformal doping [9]. In fact, conventional

* Corresponding author.
E-mail address: fuccio@laas.fr (F. Cristiano).
[1] Now with IMEC, Kapeldreef 75, 3001 Leuven, Belgium.

http://dx.doi.org/10.1016/j.mssp.2015.09.011
1369-8001/

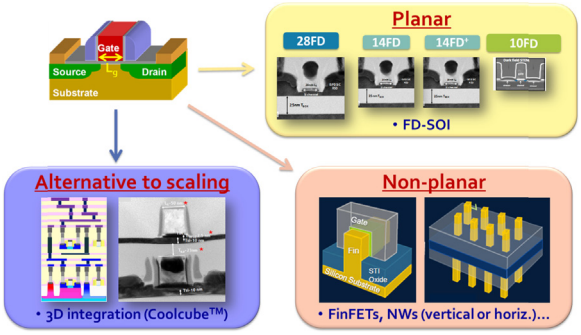

Fig. 1. Schematic description of several advanced MOS transistor architectures: planar FD-SOI (courtesy of M.Vinet, CEA-LETI), 3D integration (© 2011 IEEE. Reprinted, with permission, from Proc. IEDM 2011 7.3.1–7.3.4), Non-planar scaling (courtesy of B. Colombeau, Applied Materials).

beamline implants can only be performed using low-angle tilted beams due to fin/photo resist shadowing [10]. Plasma immersion ion implantation [11,12] or other plasma-related doping methods [13,14] are the most promising candidates to improve conformality in fin doping [15]. Finally, it is important to note that dopant conformality is a critical issue also for CMOS imagers, where deep trench isolation between neighbour MOS cells is achieved by forming shallow doped junctions at the surfaces of the trenches [16].

Nanowire-based field effect transistors (NW-FETs) are among the most promising solutions to overcome the limits of today's electronic devices, especially for their ability to implement gate-all-around architectures [17]. NW doping can be achieved *in-situ* during growth [18] or *ex-situ* following several methods (diffusion [19], molecular doping [20,21], ion implantation [22]), However, the efficiency of each one of these methods critically depends on several parameters and physical phenomena [23,24], including NW material, size or surface passivation. As a consequence, while alternative *doping-free* S/D fabrication schemes based on the implementation of "Schottky contacts" are being developed [25], reliable and systematic studies of ion implantation-doped NWs are still lacking. Indeed, opposite results show either a reduced amount of structural disorder in implanted Si-NWs compared to bulk Si [26] or an "unrecoverable" amorphisation damage during annealing [7].

A crucial step in the fabrication of S/D doped region is the thermal anneal required for damage recovery and dopant activation. In parallel to the evolution of device architectures, thermal annealing has also evolved during the last decade towards shorter cycles combined with higher temperatures, so to combine controllable diffusion with high activation [27]. Currently used "spike" Rapid Thermal Anneals (RTA), with ramping rates in the order of 250 °C/s, are expected to be replaced with even faster methods operating in the millisecond or nanosecond scale. In particular, the recent advances in nanosecond laser annealing have opened the way to solve a wide spectrum of difficult challenges in semiconductor technology, well beyond the S/D fabrication issues. Indeed, thanks to the low thermal budget of a laser pulse (with duration in the nanosecond regime), laser annealing is very attractive not only for the achievement of abrupt junctions [28,29,30], but more generally for all semiconductor technologies in which dopants need to be activated while preserving the integrity of the surrounding areas, as in the case of thin film displays [31], high-frequency bipolar silicon-on-glass processes [32], CMOS backside imagers [33,34] or 3D integration schemes [35,36], for which localised laser annealing is a promising alternative to low temperature (<600 °C) Solid Phase Epitaxy processes [37].

However, several issues still need to be investigated to achieve a thorough understanding of the underlying physics, improve the predictive modelling of dopant redistribution during laser process and ultimately optimise the process conditions. They range from the non-uniform absorption of the radiation up to the kinetically limited segregation of dopants and intrinsic point defects during liquid-phase epitaxy. A particularly important challenge is the role of residual damage on the activation of dopants, its evolution during laser processing and its stability during post-implantation annealing at lower temperatures.

In this paper, we will focus on damage related issues, by presenting some recent investigations focused on damage evolution and its impact on dopant distribution and electrical activation during nanosecond laser thermal annealing of ion implanted group IV semiconductors. Section 2 will concern Si, while recent results on Germanium will be reported in Section 3.

2. Silicon

In this section, we report our recent investigations [38–40] on the formation of extended defects and their impact on dopant activation during nanosecond laser thermal annealing in non-melt, partial melt and full melt conditions of Boron implanted silicon. These results show that, in the case of non-melt anneals, the resulting large defects can act as scattering centres, leading to a degradation of carrier mobility. In contrast, in the case of melt anneal conditions, it is shown that the molten region itself is of excellent crystalline quality, free of any large defects and leads to very high activation rates.

2.1. Experimental details

A CZ *n*-type (001) Si wafer was implanted with 30 keV B^+ to a dose of 1×10^{15} cm^{-2}. Several pieces of the implanted wafer were annealed under excimer laser radiation ($\lambda=308$ nm, pulse duration <200 ns), with laser energy densities ranging from 1.5 J/cm^2 to 2.9 J/cm^2 and different numbers of pulses (from 1 to 10). These conditions correspond to different regimes of the annealing process, including non-melt, partial melt (with respect to the depth of the mean projected range, R_p, of the implanted dopant) and full melt of the implanted profile. B^+ concentration profiles were analysed by Secondary Ion Mass Spectrometry (SIMS), while Hall measurements were carried out on an Accent HL5500 Hall effect system. Raw data were analysed using the method described in Ref. [41], in order to extract additional information about the dopant activation level and estimate any mobility degradation induced by the defects. Finally, the annealed samples were analysed by Transmission Electron Microscopy (TEM) in plan-view and cross-sectional configuration. Several imaging techniques were used for the TEM investigations, including Weak Beam Dark Field (WBDF), high-resolution (HREM) and geometric phase analysis.

2.2. Dopant distribution and defect formation

Boron concentration profiles measured by SIMS for several laser annealing conditions are reported in Fig. 2. After a non-melt anneal (1.5 J/cm^2, not shown) the Boron profile is not modified compared to the as-implanted one, and this independently of the number of laser pulses. In contrast, strong dopant redistribution occurs at higher laser energy densities, producing progressively thicker melted regions. In particular, a plateau is formed in the melted region. No Boron diffusion is observed below the liquid/solid (l/s) interface. All of the observed features can be well explained as a consequence of dopant adsorption at the l/s interface during solidification [42].

Fig. 3 reports cross-section TEM images from B^+ implanted

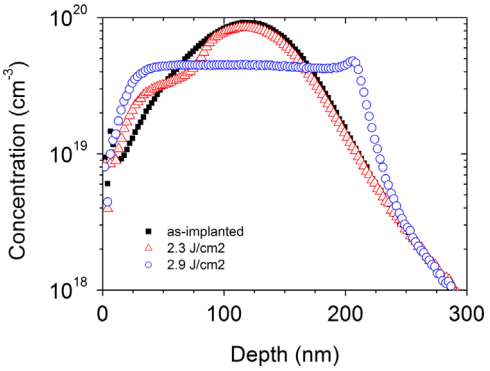

Fig. 2. SIMS boron profiles from B implanted samples annealed by laser annealing at different energy densities.

samples laser annealed by (a) 1 pulse at 2.3 J/cm^2 (partial melt above the R_p) or (b) 1 pulse at 2.6 J/cm^2 (partial melt beyond the R_p). In such "partial melt" cases, the upper limit of the defect regions corresponds to the position of the l/s interface, indicating that the defects are formed in the solid phase just below the melted region. In addition, the apparent defect size is found to decrease with increasing depth (not shown). This result is in agreement with the rapid decrease of the substrate temperature below the melted region [43,44]. In the non-melt case (not shown), the defect band is instead found to occupy a relatively wide region (~150 nm) centred at the boron projected range, R_p, which is typical of "non-melt" anneals of samples implanted below the amorphisation threshold. In all cases, it was found that all observed defects exhibit a loop-like contrast (cf. inset in Fig. 3b). Finally, no defects are observed in the sample with a melted region extending well beyond the implanted profile.

The nature of the observed defects has been extensively investigated [39] using both the $g \cdot b$ defect contrast method as well as the Geometric Phase Analysis (GPA) of HREM images. In particular, it was possible to determine the Burgers vector direction, b, as well as the habit plane of the observed loops. It was found that, unlikely the conventional RTA anneal case, most of the loops have a Burgers vector parallel to the [001] direction and a habit plane parallel to the (001) surface, *i.e.* they are different from the conventional loops typically observed in ion implanted silicon (all lying on {111} planes and with Burgers vectors of $1/2 <110>$ or $1/3 <111>$). A summary of the quantitative analysis of the TEM images is reported in Fig. 4, indicating that, within the total defect population, the fraction of (001) DLs increases from about 60% in the sample annealed with 2.3 J/cm^2 laser energy, up to almost 100% in the sample annealed with a laser energy of 2.6 J/cm^2.

The results shown in this work clearly indicate that a modification of the defect formation energy occurs during laser annealing, compared to conventional RTA anneals. The observed behaviour was explained [39] in terms of the modification of the defect formation energy induced by the compressive biaxial stress developed in the non-melted regions during laser annealing. Indeed, during laser annealing, the strong temperature gradients existing between the top-most solid region (immediately below the free surface or the l/s interface, depending on the anneal conditions) and the deeper substrate regions are expected to induce a depth-dependant lattice parameter modification and a corresponding compressive biaxial stress field, which in turn can affect the defect formation energy [45,46]. This hypothesis was confirmed by our calculations based on the combination of the phase-field methodology [47] (for the simulation of the temperature T and phase field Φ) with the thermo-elastic theory. The computed stress variation was then used to calculate the formation energy of the various loop types. Indeed, it was found that, when calculated at the time of maximum compressive stress, the formation energy of conventional {111} loops overcomes that of (001) loops. The latters therefore become the most favourable defect configuration during ultra-fast laser annealing, in agreement with the observed results.

2.3. Defect impact on dopant activation

In this last section, we investigate the evolution of dopant activation in B^+ implanted Si following a ns anneal, in order to assess the possible impact of the (001) loops on carrier mobility. The sheet resistance values of the investigated samples are reported in Fig. 5a (circles) and clearly show that with the exception of the samples annealed in non-melt conditions (1.5 J/cm^2) the sheet resistance is systematically lower than 200 Ω/sq in all annealed samples, with values that continuously decrease when the thermal budget is increased (laser energy or number of pulses). This behaviour is essentially due to the increase of the dopant active dose (Fig. 5b, circles), while the hole mobility is only weakly modified by the various annealing conditions (Fig. 5c, circles). It has to be noted that the reference RTA annealed sample (900 °C 10 min) exhibits a low sheet resistance similar to those obtained after laser anneals. However, a strong diffusion of the Boron profile occurs in

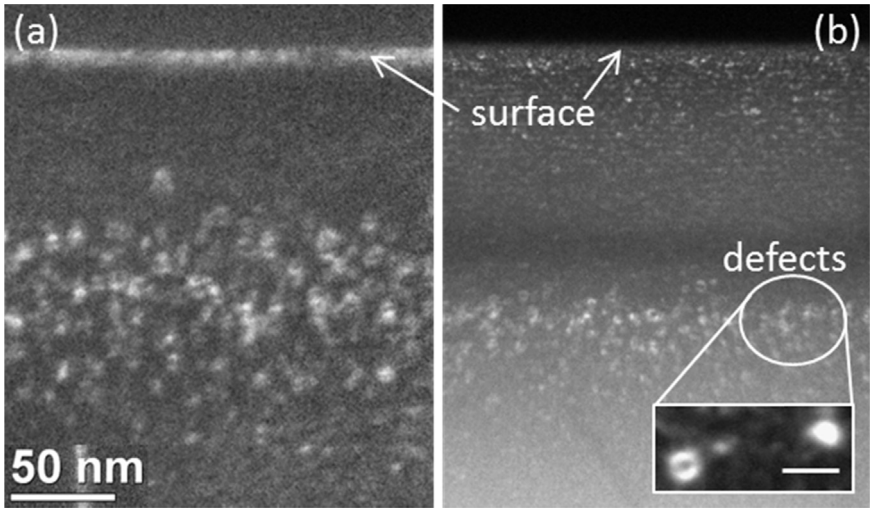

Fig. 3. Cross-section TEM images from B implanted samples annealed by (a) 1 pulse at 2.3 J/cm^2 (partial melt above the R_p) or (b) 1 pulse at 2.6 J/cm^2 (partial melt beyond the R_p). Scale bar in the inset: 20 nm.

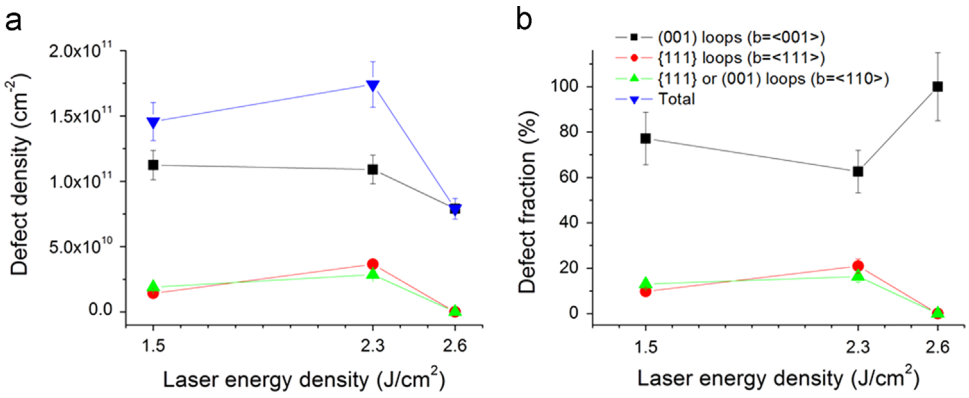

Fig. 4. Contribution of the different defect types to the total defect population in B^+-implanted samples after laser annealing at different energy densities. (a) Areal density of defects. (b) Fraction of each defect type with respect to the total population.

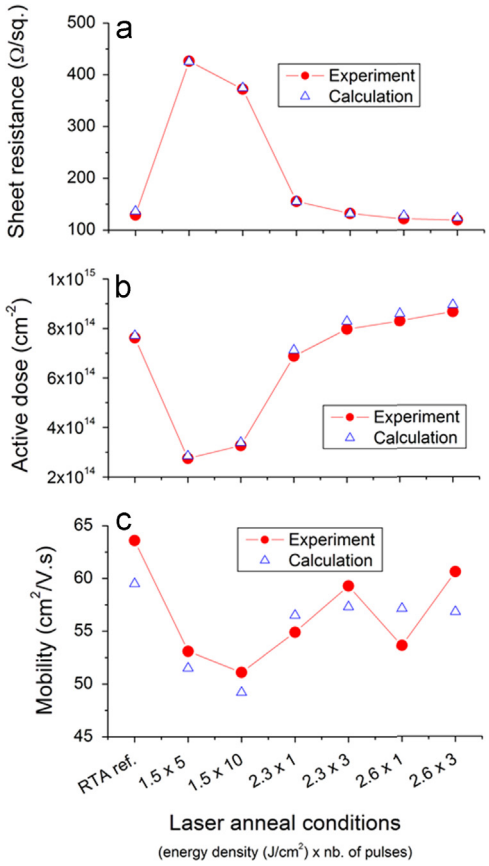

Fig. 5. Sheet resistance (a), dopant active dose (b) and mobility (c) as a function of the annealing conditions (laser energy in J/cm^2 × nb of pulses). Circles: experiments. Triangles: calculations.

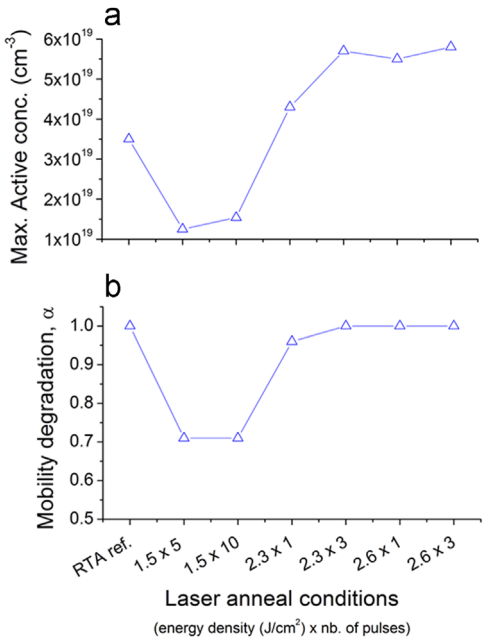

Fig. 6. Maximum active concentration (a) and mobility degradation coefficient (b) as a function of the annealing conditions (laser energy in J/cm^2 × nb of shots). The values reported in these plots allow to perfectly reproduce the Hall effect measurements reported in Fig. 5 (© 2014 IEEE. Reprinted, with permission, from F. Cristiano et al., Proc. IWJT 2014).

this sample (not shown), with an in-depth shift of ~70 nm at 10^{18} cm^{-3}, whereas the tail of the Boron profile does not diffuse at all after laser anneal.

Using the method of analysis described in [41], it is possible to estimate the best values of the maximum active concentration, C_{el}, and of the mobility degradation coefficient, α, that allow to perfectly reproduce the Hall effect measurements. In practice, the C_{el} value is first determined in order to fit the active dose (cf. triangles in Fig. 5b). The α value is then adjusted in order to calculate the sheet resistance (triangles in Fig. 5a) and the carrier mobility (triangles in Fig. 5c) in all the annealed samples. The best fit C_{el} and α values are reported in Fig. 6. It is found (Fig. 6a) that after a low energy non-melt anneal (1.5 J/cm^2), the C_{el} is as low as 1.2×10^{19} (after 5 pulses), indicating that most of the implanted Boron dose (~70%) is electrically inactive. With increasing thermal budget, the C_{el} value rapidly stabilises at values between 5 and 6×10^{19} cm^{-3}, corresponding to active doses approaching 90%.

Finally, it is important to note that no mobility degradation is estimated in samples that have undergone a melt laser process (2.3 and 2.6 J/cm^2) ($\alpha \sim 1$, Fig. 6b). In contrast, it was necessary to assume a 30% mobility reduction ($\alpha \sim 0.7$) with respect to the standard values in order to match the Hall effect measurements obtained from the samples annealed in non-melt conditions. If such mobility degradation is not considered, the calculated value of sheet resistance for the "1.5 J/cm^2 5 pulses" annealed sample would be 302 Ω/sq. (instead of 426, see Fig. 5a). Similarly, the calculated mobility value for the same sample would be 73 cm^2/V s (instead of the measured 53 cm^2/V, see Fig. 5c).

The strong mobility degradation in the non-melt samples is a clear evidence that the (001) loops, which are uniformly distributed within the implanted Boron profile, act as additional bulk scattering centres, similarly to what was previously found for BICs [41]. In contrast, in the case of melt annealing conditions, no

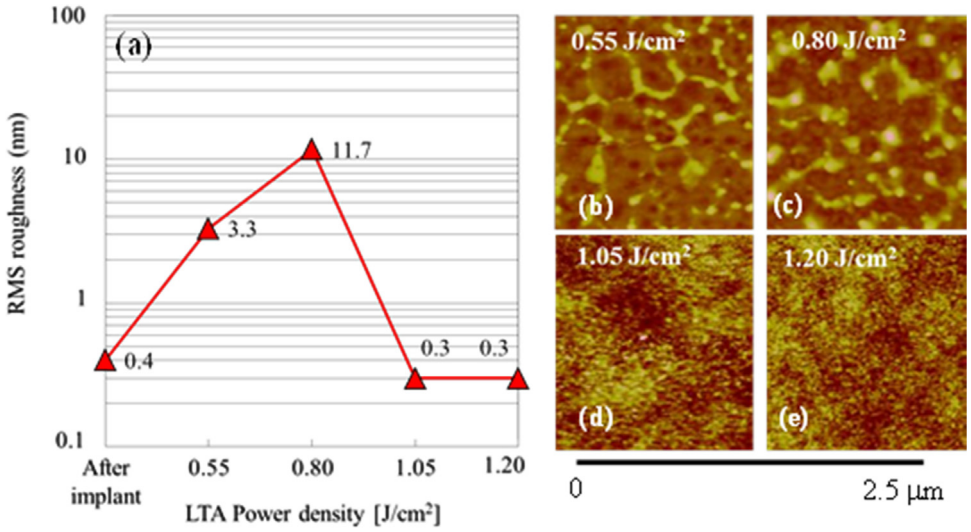

Fig. 7. Surface roughness (a) and corresponding AFM images (b) versus laser energy density.

mobility degradation needed to be assumed in order to reproduce the measured values, and this despite (001) loops are also present in these samples (cf Fig. 4). This apparently different behaviour can be explained considering that Hall measurements are based on current flowing through surface contacts. In non-melt case, as seen by TEM analysis, many defects remain near the surface, thus impacting the Hall measurement by a significant degradation of the Hall mobility. In contrast, in the partial and full melt cases, the surface region, in which most of the activated dopants are contained, is perfectly recrystallised. Hence, no significant contribution to the measurements can arise from the defect layer, located far below the surface, within the buried and lowly doped region of the samples. As a consequence, the absence of mobility degradation in melt annealed samples cannot be associated to a weak impact of the defects, but it is to be interpreted as a proof of the high electrical quality of the recrystallised layer.

3. Germanium

Nowadays, there is a renewed interest in the use of Ge for advanced CMOS technology because of its superior electrical characteristics and lower temperature processes compared to Si, as well as its compatibility with the well-established silicon technology. Indeed, the interest in using Germanium to replace Si as a high-mobility channel material was triggered in the early 2000s by the successful implementation of high-k dielectrics to replace SiO_2 in Si MOS [48,49]. Since then, the feasibility of high-performing p-channel Ge devices has been demonstrated [50] while good performing n-channel devices remain an issue [51].

Recently, Laser thermal annealing (LTA) process has been demonstrated as a formidable process to achieve very high As doping in Ge, well above the solid solubility limit in Ge [52,53]. However, the structure modification induced by LTA in very thin amorphised Ge layers and its correlation with the electrical properties is still missing. In this paper, we studied in detail the amorphous to crystalline Ge phase transition as a function of the increasing LTA energy density and we found that using LTA, very high carrier concentrations (above 10^{20} cm^{-3}) were achieved in As doped regions when the amorphised material was perfectly recrystallised.

3.1. Experimental details

Ge Czochralski wafers, (100)-oriented, (p-type 0.059–0.088 Ω cm) were implanted with 28 keV As^+ ions to a dose of 2×10^{15} cm^{-2}, above the amorphisation threshold. In order to study the thermal effect of LTA, the as-implanted samples were cut into small pieces and were subjected to various treatments (single pulse, $\lambda = 308$ nm) at different energy densities: i.e. 0.55 J/cm^2 (corresponding to the onset of Ge surface melting), 0.80 J/cm^2, 1.05 J/cm^2, and 1.20 J/cm^2. Further details on the laser treatments are reported elsewhere [53].

The surface morphology was investigated by Atomic Force Microscopy (AFM) in non-contact tapping mode at room temperature on 5×5 μm^2 area for surface examination and surface roughness measurements (RMS) before and after the laser processes. Micro-Raman spectra were taken in backscattering geometry with a HORIBA Jobin-Yvon system, equipped with Olympus BX41 microscope. He–Ne laser radiation at a wavelength of 632.8 nm is focused to a spot size of about 3 μm by a 100x. The laser power on the sample was about 6 mW, and a 550 mm focal length spectrometer with 1800 lines/mm grating was used. Calibration was performed with a Ge wafer by utilising the first order Raman spectrum, detecting Ge TO phonon band at $k \sim 0$. (phonon energy $E_{ph} = 37$ meV) at 301 cm^{-1}. Moreover, in order to monitor a possible local temperature increase due to the laser irradiation, we acquired both the Stokes and anti-Stokes peaks from all samples [54]. Their ratio was found to be almost constant for each sample (not shown), so that local heating of the samples during the analysis could be excluded.

TEM analyses were performed with a 200 keV 2010 JEOL and a 200 keV 2010F JEOL instruments at the IMM microscopy facilities in Catania to observe the structural effects induced by LTA as a function of the energy density. Cross-section (CS) samples were prepared by means of standard preparation with mechanical grinding and ion milling performed in a GATAN-PIPS apparatus at low energy (3 keV Ar) and low incidence angle (7°) to minimise the irradiation damage.

3.2. Results and discussion

The evolution of the surface morphology as a function of the LTA treatments is evidenced by the AFM images shown in Fig. 7b–e, while the quantitative evaluation of the roughness is reported in the graph in Fig. 7a. The RMS demonstrates that after implantation the RMS was approximately 0.3 nm, while with application of LTA at the lower energy densities (0.55 and 0.80 J/cm^2) the roughness strongly increases up to ~10 nm, indicating an abrupt worsening

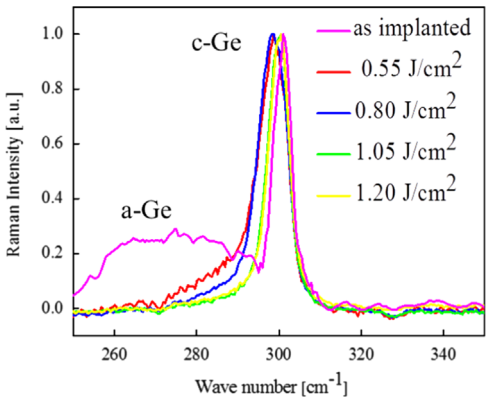

Fig. 8. Raman Stokes spectra as a function of the LTA treatments at various energy densities. (For interpretation of the references to colour in the text, the reader is referred to the web version of this article.)

of the surface. Finally, after treatments at 1.05 and 1.20 J/cm^2 an almost flat surface is restored. The AFM measurements clearly demonstrate that only high density energy processes resulted in an perfectly planar surface, while it appears to be strongly damaged after low energy LTA.

The morphological characteristics deduced from the AFM measurements have their counterpart in the bulk properties investigated by Raman spectroscopy, which was used to study the degree of structural disorder on a large scale. The Raman Stokes peaks measured after different LTA processes are reported in Fig. 8 where the evolution of spectra from the amorphous phase to the crystalline one is clearly evidenced. Indeed, the Stokes spectrum corresponding to the as implanted sample presents a broad band centred at 270 cm^{-1} assigned to the transverse optical mode in amorphous Ge [55] and a sharp peak at 301 cm^{-1} corresponding to Ge–Ge vibrational modes in crystalline Ge [56]. Since the laser penetration depth in Ge is about 50 nm, these results indicate that the two Raman signals are related, respectively, to the top layer of the Ge amorphised by the As implantation and by the underlying crystalline Ge bulk. Moreover, after LTA anneal with progressively increasing energy, we note a strong reduction of the amorphous contribution indicating a gradual recrystallisation of the amorphous layer and, correspondingly, a progressive energy shift and width narrowing of the Raman peak. Indeed, the peak at 301 cm^{-1} shifts from 298.7 to 300.5 cm^{-1} while the full width at half maximum (FWHM) decreases from 7.9 to 5.6 cm^{-1}. Considering that when the long range order is progressively restored the FWHM progressively shrinks [56], we may conclude that on sample annealed at low energy densities (0.55 and 0.80 J/cm^2) an internal structural disorder is still present and it is recovered only after LTA processes at 1.05 and 1.20 J/cm^2.

Finally, with the aim to correlate the long range analyses (AFM and Raman spectroscopy) with the microscopically structure of samples, we performed CS-TEM analyses on selected samples subjected to various LTA annealing. In Fig. 9a, a CS view of the as-implanted sample shows the location of the amorphous–crystalline (a–c) interface at about 35–40 nm below the surface, in close agreement with the Raman spectra reported in Fig. 8 (purple line). In addition, although the a–c interface exhibits a roughness of ~5 nm, the amorphous surface appears almost flat in agreement with the RSM value measured by AFM and reported in Fig. 7. After the LTA at 0.55 J/cm^2 (Fig. 9b) the implant damage was only partially recovered, through the formation of a polycrystalline material containing embedded amorphous pockets (few tens on nm large), as shown in the high resolution (HR-TEM) image acquired in correspondence of a Ge grain boundary reported in the inset of Fig. 9b.

A similar polycrystalline structure has been observed on the sample annealed at 0.80 J/cm^2 even if in this case the presence of amorphous Ge is completely excluded, as shown in the TEM image in Fig. 9c. The observation of a polycrystalline structure after LTA processes at energy density values up to 0.8 J/cm^2 is assigned to the fact that under these conditions the liquid–solid interface remains within the initial amorphous Ge layer. In such case, the rapid cooling of the melted region induces the random nucleation of small Ge grains within the amorphous matrix that can evolve towards a fully polycrystalline structure. The observation of a disordered structures composed by nanocrystalline grains is in agreement with the broad FWHM of the corresponding Raman spectra (red and blue lines in Fig. 8). Finally, the epitaxial

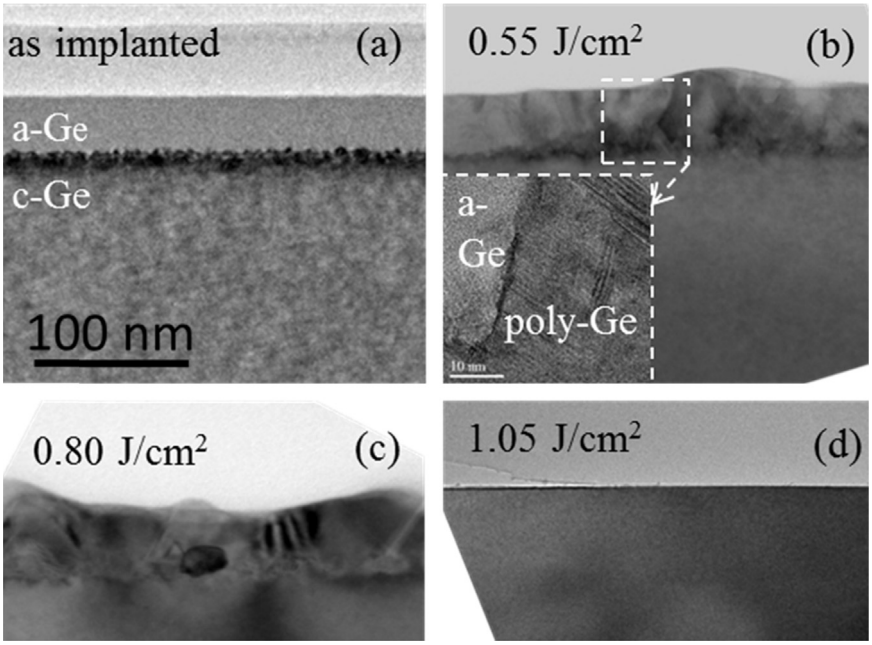

Fig. 9. CS-TEM of as-implanted (a) and LTA Ge at 0.55 (b), 0.8 (c) and 1.05 J/cm^2 (d). In the inset of (b) a HR-TEM taken in correspondence of the grain boundary shows the presence of amorphous pockets (a-Ge).

recrystallisation is reached after the high laser density annealing which induced the melting below the a/c interface, as shown by TEM analyses of the sample annealed at 1.05 J/cm^2 reported in Fig. 9d, and confirmed by the shrinking of the Raman spectra (green and yellow spectra in Fig. 8).

Micro Hall effect measurements were performed on the fully recrystallised samples (LTA energy of 1.05 and 1.2 J/cm^2), and compared with SIMS concentration profiles, as reported in ref. [53]. Within the experimental errors of the SIMS measurements, the total As dose was the same in the two samples ($\sim 9 \times 10^{14}$ cm^{-2}). In contrast, the increased melt depth induced by the higher LTA energy process results in a deeper doped region with a lower dopant concentration ($\sim 1 \times 10^{20}$ cm^{-3} after 1.2 J/cm^2 vs. $\sim 2 \times 10^{20}$ cm^{-3} after 1.05 J/cm^2). The corresponding Hall effect measurements indicated that a full dopant activation is achieved in both cases ($\sim 9 \times 10^{14}$ cm^{-2}), confirming that the active concentrations as high as $\sim 1 \times 10^{20}$ cm^{-3} can be achieved for n-type dopants in Ge by melt laser anneal. Finally, the Hall mobility and sheet resistance values were found to be in agreement with the dopant profile evolution measured by SIMS. Indeed, the carrier mobility was found to increase from 94 cm^2/Vs after 1.05 J/cm^2 LTA to 112 cm^2/Vs after 1.20 J/cm^2 LTA (in agreement with a lower dopant concentration at 1.20 J/cm^2), leading to an overall decrease of the sheet resistance ($\sim 75\ \Omega$/sq. to $\sim 65\ \Omega$/sq) when the laser energy was increased from 1.05 to 1.20 J/cm^2.

In conclusion from the extensive microscopical structural analyses, it is evident that at low laser energy densities, a residual disorder is observed in the crystal, while at high energy density, crystalline integrity is restored. This results in extremely high levels of active dopant concentration, unachievable with conventional RTA processes.

4. Conclusions

During the last decade, the miniaturisation of planar “bulk Si” MOS transistors through the purely geometrical scaling approach has reached its limits. This has resulted in a considerable diversification of the possible device architectures for future technology nodes. Planar FD-SOI transistors, 3D multigate FinFETs and gate-all-around nanowire FETs are briefly reviewed in terms of the doping requirements related to the fabrication of source/drain (S/D) regions. The growing interest in the use of ultra-fast laser annealing for the achievement of abrupt and highly doped junctions is then discussed and some recent investigations focused on laser annealing, with particular emphasis on the investigation of the formation and evolution of implant/anneal induced defects and their impact on dopant activation.

In the case of laser annealed Silicon (Section 2), by a careful interpretation and confrontation of TEM, SIMS, and Hall effect measurements, it is found that laser anneal favours the formation of “unconventional” (001) loops which are typically not expected to occur in ion implanted silicon. Following non-melt anneals, these loops act as carrier scattering centres, leading to carrier mobility degradation. In contrast, in the case of melt anneals, the molten region itself is of excellent crystalline quality, free of any large defects and leads to very high activation rates. Full melting of the implanted region leads to an almost perfectly recrystallised layer.

As for laser annealed Germanium (Section 3), we studied in detail the amorphous to crystalline Ge phase transition as a function of the increasing LTA energy density and we found that using LTA, very high carrier concentrations (above 10^{20} cm^{-3}) were achieved in As doped regions, which are unachievable with conventional RTA processes, provided the amorphised material was perfectly recrystallised.

Acknowledgements

The research activity on laser annealed Silicon (Section 2) received funding from the European Union Seventh Framework Programme (FP7/2007-2013) under grant agreement no. 258547 (ATEMOX). The research activity on laser annealed Germanium (Section 3) was supported in part by the Higher Education Authority Programme for Research in Third-Level Institutions in Ireland under grant agreement no. "HEA PRTLI5".

References

[1] H. Iwai, Microelectron. Eng. 86 (2009) 1520–1528.
[2] M. Vinet, et al. Proceedings of the VLSI-TSA Meeting, 2012.
[3] L. Hutin, et al., Proceedings of the IEEE International Workshop on Junction Technology, S7-04, 2014.
[4] B. Colombeau, et al., Phys. Status Solidi A 211 (2014) 101.
[5] G. Larrieu, et al., in: Proceedings of the International Electron Devices Meeting'07, 2007, pp. 147–150.
[6] F.A. Khaja, et al., Proceedings of the AIP Conference on IIT, 1496, 2012, p. 42.
[7] R. Duffy, M.J.H. Van Dal, B.J. Pawlak, M. Kaiser, R.G.R. Weemaes, B. Degroote, E. Kunnen, E. Altamirano, Appl. Phys. Lett. 90 (2007) 241912.
[8] M. Togo, et al., IEEE VLSI Conference 2013, Paper 14–2, p. T196.
[9] W. Vandervorst, et al., Proceedings of the AIP Conference Proceedings on IIT , 1066, 2008, p. 449.
[10] N. Horiguchi, et al., Proceedings of the IEEE International Workshop on Junction Technology, I3-2, 2012.
[11] J. Duchaine, et al., Proceedings of the AIP Conference on IIT, 1496, 2012, p. 71.
[12] F. Gonzatti, F. Milési, V. Delaye, J. Duchaine, F. Torregrosa, H. Etienne, K. Yckache, in: J. Matsuo et al. (Ed.), Proceedings of the AIP on IIT10, 2010, p. 27.
[13] Y. Sasaki, et al., J. Appl. Phys. 111 (2012) 013712.
[14] J.W. Lee, et al., Appl. Phys. Lett. 102 (2013) 223508.
[15] G. Zschatzsch, et al., IEEE IEDM Technical Digest, 2011, p. 841.
[16] F. Roy, et al., Phys. Status Solidi C 11 (2014) 50.
[17] J. Appenzeller, J. Knoch, M.T. Björk, H. Riel, H. Schmid, W. Riess, IEEE Trans. Electron Dev. 55 (2008) 2827.
[18] D.E. Perea, et al., Nat. Nanotechnol. 4 (2009) 315.
[19] E.C. Garnett, et al., Nat. Nanotechnol. 4 (2009) 311.
[20] J.C. Ho, et al., Nano Lett. 9 (2009) 725.
[21] R.A. Puglisi, C. Garozzo, C. Bongiorno, S. DiFranco, M. Italia, G. Mannino, S. Scalese, A. LaMagna, Solar Energy Mat. & Solar Cells 132 (2015) 118.
[22] W. Paschoal, et al., Nano Lett. 12 (2012) 4838.
[23] V. Scmhidt, et al., Adv. Mater. 21 (2009) 1.
[24] C. Ronning, et al., Mater. Sci. Eng. R 70 (2010) 30.
[25] G. Larrieu, X.L. Han, Nanoscale 5 (2013) 2437–2441.
[26] A. Colli, A. Fasoli, C. Ronning, S. Pisana, S. Piscanec, A.C. Ferrari, Nano Lett. 8 (2008) 2188.
[27] A.T. Fiory, K.K. Bourdelle, Appl. Phys. Lett. 74 (1999) 2658.
[28] Y. Takamura, S.H. Jain, P.B. Griffin, J.D. Plummer, J. Appl. Phys. 92 (2002) 230.
[29] E.V. Monakhov, B.G. Svensson, M.K. Linnarsson, A. La Magna, V. Privitera, M. Camalleri, G. Fortunato, L. Mariucci, Mater. Sci. Eng. B 114–115 (2004) 352.
[30] S.W. Do, S.H. Kong, Y.H. Lee, J.G. Oh, J.K. Lee, M.A. Ju, S.J. Jeon, J.C. Ku, J. Korean Phys. Soc. 55 (2009) 1065.
[31] A.T. Voutsas, M.K. Hatalis, Technology of polysilicon thin-film transistors, in: C. R. Kagan, P. Andry (Eds.), Thin Film Transistors, Marcel Dekker, New York, 2003, pp. 139–207.
[32] G. Lorito, V. Gonda, S. Liu, T.L.M. Scholtes, H. Schellevis, L.K. Nanver, Proceedings of the IEEE 2006 International Conference on Microelectronics, MIEL, vol. 25, 2006, p. 342.
[33] H. Bourdon, A. Halimaoui, J. Venturini, F. Gonzatti, D. Dutartre, 15th International Conference on Advanced Thermal Processing of Semiconductors, Catania, 2007, p. 275.
[34] K. Huet, et al., Proceedings of the 19th International Conference on Ion Implementation Technology, AIP Conference Proceeding, 1496, 2012, pp. 135 – 138.
[35] B. Rajendran, R.S. Shenoy, M.O. Thompson, R.F.W. Pease, Proceedings of the 2004 VLSI Multilevel Interconnection Conference, IEEE 2004.
[36] P. Batude, M. Vinet, B. Previtali, C. Tabone, C. Xu, J. Mazurier, O. Weber, F. Andrieu, L. Tosti, L. Brevard, B. Sklenard, P. Coudrain, S. Bobba, H. Ben Jamaa, P. Gaillardon, A. Pouydebasque, O. Thomas, C. Le Royer, J. Hartmann, L. Sanchez, L. Baud, V. Carron, L. Clavelier, G. De Micheli, S. Deleonibus, O. Faynot, T. Poiroux, IEDM 2011, pp. 7.3.1–7.3.4.
[37] C. Fenouillet-Beranger, B. Previtali, P. Batude, F. Nemouchi, M. Cassé, X. Garros, L. Tosti, N. Rambal, D. Lafond, H. Dansas, L. Pasini, L. Brunet, F. Deprat, M. Grégoire, M. Mellier, M. Vinet, IEDM, 2014, p. 110.
[38] G. Fisicaro, L. Pelaz, M. Aboy, P. Lopez, M. Italia, K. Huet, F. Cristiano, Z. Essa, Y. Qiu, E. Bedel-Pereira, M. Quillec, A. La Magna, App. Phys. Express 7 (2014) 021301.
[39] Y. Qiu, F. Cristiano, K. Huet, F. Mazzamuto, G. Fisicaro, A. La Magna, M. Quillec, N. Cherkashin, H. Wang, S. Duguay, D. Blavette, Nano Lett. 14 (2014) 1769.
[40] F. Cristiano, Y. Qiu, E. Bedel-Pereira, K. Huet, F. Mazzamuto, G. Fisicaro, A. La

Magna, M. Quillec, N. Cherkashin, H. Wang, S. Duguay, D. Blavette, Proceedings of the 14th International Workshop Junction Technology (IWJT 2014), May 2014, IEEE, Shanghai, 2014, pp. 7–12.
[41] F. Severac, F. Cristiano, E. Bedel-Pereira, P.F. Fazzini, J. Boucher, W. Lerch, S. Hamm, J. Appl. Phys. 107 (2010) 123711.
[42] G. Fisicaro, K. Huet, R. Negru, M. Hackenberg, P. Pichler, N. Taleb, A. La Magna, Phys. Rev. Lett. 110 (2013) 117801.
[43] M. Hackenberg, P. Pichler, K. Huet, R. Negru, J. Venturini, A. Pakfar, C. Tavernier, A. La Magna., Appl. Surf. Sci. 28 (2012) 9347.
[44] G. Fisicaro, L. Pelaz, P. Lòpez, A. La Magna, Phys. Rev. E 86 (2012) 036705.
[45] A.J. Pitera, E.A. Fitzgerald, J. Appl. Phys. 97 (2005) 104511.
[46] M. Nastasi, T. Höchbauer, J.-K. Lee, A. Misra, J.P. Hirth, M. Ridgway, T. Lafford, Appl. Phys. Lett. 86 (2005) 154102.
[47] K. Huet, G. Fisicaro, J. Venturini, H. Besaucèle, A. La Magna, Appl. Phys. Lett. 95 (2009) 231901.
[48] B.H. Lee, J.W. Oh, H.H. Tseng, R. Jammy, H. Huff, Mater. Today 9 (2006) 32.
[49] C. Claeys, E. Simoen, K. Opsomer, D.P. Brunco, M. Meuris, Mater. Sci. Eng. B 154 (2008) 49.
[50] J. Mitard, B. De Jaeger, F.E. Leys, G. Hellings, K. Martens, G. Eneman, D.P. Brunco, R. Loo, J.C. Lin, D. Shamiryan, T. Vandeweyer, G. Winderickx, E. Vrancken, C.H. Yu, K. De Meyer, M. Caymax, L. Pantisano, M. Meuris, M.M. Heyns, IEDM Technical Digest, 2008, p. 873.
[51] Y. Song, H. Zhou, Q. Xu, J. Luo, H. Yin, J. Yan, H. Zhong, J. Electron. Mater. 40 (2011) 1584–1612.
[52] R. Milazzo, E. Napolitani, G. Impellizzeri, G. Fisicaro, S. Boninelli, M. Cuscunà, D. De Salvador, M. Mastromatteo, M. Italia, A. La Magna, G. Fortunato, F. Priolo, V. Privitera, A. Carnera, J. Appl. Phys. 115 (2014) 053501.
[53] M. Shayesteh, D. O'Connell, F. Gity, P. Murphy-Armando, R. Yu, K. Huet, I. Toqué-Tresonne, F. Cristiano, S. Boninelli, H. Hartmann Henrichsen, P. Folmer Nielsen, D. Hjorth Petersen, R. Duffy, IEEE Trans. Electron Dev. 61 (2014) 4047.
[54] G. Faraci, S. Gibilisco, A.R. Pennisi, Phys. Rev. B 80 (2009) 193410.
[55] M. Wihl, M. Cardona, J. Tauc, J. Non-Cryst. Solids 8–10 (1972) 172–178.
[56] R. Carles, A. Mlayah, M. Amjoud, M. Amjoud, A. Reines, R. Morancho, Jpn. J. Appl. Phys. 31 (11) (1992) 3511–3514.tp